

Brain-Decellularized ECM-Based 3D Myeloid Sarcoma Platform: Mimicking Adaptive Phenotypic Alterations in the Brain

Heejeong Yoon, Joo H. Kang, Seung Woo Cho, Chun Gwon Park, Dong-Wook Kim,* and Tae-Eun Park*

Leukemia circulates in the bloodstream and induces various symptoms and complications. Occasionally, these cells accumulate in non-marrow tissues, forming a tumor-like myeloid sarcoma (MS). When the blast-stage leukemia cells invade the brain parenchyma, intracranial MS occurs, leading to a challenging prognosis owing to the limited penetration of cytostatic drugs into the brain and the development of drug resistance. The scarcity of tissue samples from MS makes understanding the phenotypic changes occurring in leukemia cells within the brain environment challenging, thereby hindering development of effective treatment strategies for intracranial MS. This study presents a novel 3D in vitro model mimicking intracranial MS, employing a hydrogel scaffold derived from the brain-decellularized extracellular matrix in which suspended leukemia cells are embedded, simulating the formation of tumor masses in the brain parenchyma. This model reveals marked phenotypic changes in leukemia cells, including altered survival, proliferation, differentiation, and cell cycle regulation. Notably, proportion of dormant leukemia stem cells increases and expression of multidrug resistance genes is upregulated, leading to imatinib resistance, mirroring the pathological features of in vivo MS tissue. Furthermore, suppression of ferroptosis is identified as an important characteristic of intracranial MS, providing valuable insights for the development of targeted therapeutic strategies.

marrow and is characterized by the presence of a BCR-ABL fusion gene on the Philadelphia chromosome.^[1] The BCR-ABL gene encodes a protein known as a tyrosine kinase that causes CML cells to proliferate uncontrollably. As a variant of blood cancer, CML cells travel throughout the body via the bloodstream, infiltrating various organs and tissues, and leading to a spectrum of symptoms and complications.^[2] However, during the blast crisis phase, characterized by a surge and accumulation of immature blood cells, CML cells can accumulate in tissues outside the bone marrow.^[3] These clusters form tumor-like structures known as myeloid sarcoma (MS) or chloroma. Previous studies have indicated a 7–17% prevalence of MS in patients undergoing CML blast crisis, with these formations primarily appearing in the lymph nodes, soft tissues, skin, and bones.^[4]

Intracranial leukemic masses can also form, albeit rarely, when blast cells infiltrate the meninges or the brain parenchyma.^[5] The prognosis of patients with intracranial MS is particularly poor because of the

limited penetration of cytostatic drugs for the treatment of leukemia across the blood–brain barrier, creating a challenging treatment environment.^[6] Furthermore, these masses often develop resistance to therapies such as tyrosine kinase inhibitors

1. Introduction

Chronic myeloid leukemia (CML) is caused by a genetic mutation in immature hematopoietic stem cells (HSCs) in the bone

H. Yoon, J. H. Kang, S. W. Cho, T.-E. Park
Department of Biomedical Engineering
College of Information and Biotechnology
Ulsan National Institute of Science and Technology (UNIST)
Ulsan 44919, Republic of Korea
E-mail: tepark@unist.ac.kr

C. G. Park
Department of Biomedical Engineering
SKKU Institute for Convergence
Sungkyunkwan University (SKKU)
Suwon 16419, Republic of Korea

 The ORCID identification number(s) for the author(s) of this article can be found under <https://doi.org/10.1002/adhm.202304371>

DOI: 10.1002/adhm.202304371

C. G. Park
Department of Intelligent Precision Healthcare Convergence, SKKU
Institute for Convergence
Sungkyunkwan University (SKKU)
Suwon 16419, Republic of Korea

D.-W. Kim
Department of Hematology
Hematology Center
Uijeongbu Eulji Medical Center
Eulji University
Uijeongbu 11750, Republic of Korea
E-mail: dwkim@eulji.ac.kr

D.-W. Kim
Leukemia Omics Research Institute
Eulji University
Uijeongbu 11750, Republic of Korea

(TKIs), which may be effective during the chronic phase of CML, further complicating treatment efforts.^[7] An in-depth understanding of the phenotypic changes in CML cells as they form masses in the brain is essential for devising efficient and personalized therapeutic strategies for intracranial MS.^[6]

The interaction between the extracellular matrix (ECM), the surrounding brain cells, and lower oxygen tension are distinctive external factors that influence intracranial MS compared to factors that influence blood-circulating CML cells.^[4b,8] CML cells may undergo genetic and epigenetic changes to adapt to the new brain environment, which can influence cellular morphology, cell cycle, differentiation, metabolic activity, and drug sensitivity.^[4b,8a,9] Numerous previous studies have revealed changes in the characteristics and behaviors of solid tumor cells during metastasis and colonization of distant tissues. Nonetheless, there is a research gap regarding brain parenchyma-infiltrated CML cells.

When tissue samples for studying intracranial MS are scarce, employing 3D *in vitro* platforms that replicate *in vivo* conditions is critical. These platforms are invaluable for observing the interactions between CML cells and the brain microenvironment in a manner that reflects their natural state. Such interactions are vital for examining intricate disease progression and for precise drug testing. Although there have been initiatives to provide a 3D microenvironment for CML cells to elucidate their behavior within the bone marrow,^[10] these studies are not directly related to MS. Nevertheless, CML cells, which typically grow in suspension cultures, exhibit altered differentiation patterns and cell cycles when placed on 3D platforms that simulate bone marrow conditions. This suggests that the microenvironment substantially affects the behavior of CML cells.

Moreover, to generate unique tissue-specific signals mediated by the ECM at secondary sites of cancer cell infiltration and colonization, researchers have extensively studied decellularized ECM (dECM)-based biomaterials.^[11] They are derived from specific tissues with cellular components removed. The dECM scaffolds retained the protein composition and bioactive molecules of the original tissue, enabling the creation of metastatic models that more accurately replicate the pathological properties. Multiple studies have indicated that cancer cells colonizing dECM scaffolds exhibit metastasis-like behaviors, including variations in cell adhesion, migration, and invasion. Despite these advances, there have been no investigations into the use of dECM scaffolds to mimic infiltrated leukemia cells in specific tissues.

In this study, we introduce a pioneering 3D intracranial MS model employing brain-dECM (bdECM)-based biomaterials. We observed phenotypic alterations in the CML cell line K562, including changes in cell survival, proliferation, differentiation, and cell cycle arrest. We also investigated the development of imatinib resistance, a TKI drug. To further elucidate the importance of interactions between CML cells and ECM proteins, we performed a comparative analysis of K562 cells embedded in alginate gel (K562-alg), which lacks biological motifs.^[12] Through comprehensive bulk RNA-seq analysis, our study revealed a novel pathological feature of intracranial MS, offering valuable insights for developing efficient therapeutic approaches for treating intracranial MS.

2. Results and Discussion

2.1. Preparation and Biochemical Characterization of bdECM

To create a 3D scaffold that mimics the brain microenvironment for intracranial MS modeling, we decellularized brains extracted from pigs by integrating physical, chemical, and enzymatic methods. Given our focus on how leukemia cells adjust to a healthy brain environment, which is a key factor in the initial stage of MS development, we selected healthy brain tissue for this purpose. bdECM was freeze-dried and dissolved in a pepsin solution at a concentration of 10 mg mL⁻¹ to form a bdECM hydrogel (Figure 1a). To verify that the brain tissue was effectively decellularized while keeping the extracellular matrix intact, the removal of cell components, such as nuclei, was demonstrated by hematoxylin and eosin (H&E) staining (Figure 1b). Further analysis showed that the bdECM had less than 1% of DNA than the original brain tissue (1.72 ng μ L⁻¹ in bdECM versus 201.0 ng μ L⁻¹ in the brain tissue, Figure 1c), proving effective DNA removal through decellularization. Although a significant decrease was observed in collagen and glycosaminoglycans (GAGs) in the bdECM due to decellularization (Figure 1c), a well-structured bdECM hydrogel exhibiting a porous internal structure was successfully formed (Figure 1a,d). Furthermore, the bdECM hydrogel exhibited a compressive modulus of 2.24 \pm 0.2 kPa at a concentration of 10 mg mL⁻¹, matching the stiffness range from 0.1 to 6.2 kPa typically observed in brain tissue.^[13] This suggests that the bdECM hydrogel can provide a stiffness that mimics the physiological microenvironment of the cells embedded within it.

When we compared the total proteins and matrisome proteins^[14] before and after decellularization (Figure S1a,b, Supporting Information), a significant overlap was observed, showing that 82.9% of the total proteins and 81.9% of the proteins remained consistent between the two sample conditions. This finding suggests that most of the ECM proteins remained during the decellularization process. Moreover, little variation was found between the two bdECMs during decellularization (Figure 1e), indicating the consistency and reproducibility of our method.

To verify the reliability of bdECM in creating a humanized intracranial MS microenvironment, we compared the proteomic profiles of bdECM and Matrigel, which are widely used ECM hydrogels. In our findings, unlike Matrigel, which is predominantly composed of matrisome proteins (98.5%), bdECM displayed a substantial presence of non-matrisome proteins, which were also identified in the native tissue (Figure S1d, Supporting Information). Further analysis revealed that the bdECM contains proteins from various subcategories, including glycoproteins, collagens, and proteoglycans. This composition aligns with that of native human brain tissue but diverges from that of Matrigel, where glycoproteins constitute 97.8% of the composition (Figure S1e,f, Supporting Information).

By conducting Gene Ontology (GO) analysis on the set of matrisome proteins within the bdECM, we identified their involvement in several biological processes (BPs). These include cell-matrix and cell-substrate adhesion, central nervous system development, and various molecular functions, including calcium ion, integrin, and receptor binding (Table S1, Supporting Information). Kyoto Encyclopedia of Genes and Genomes

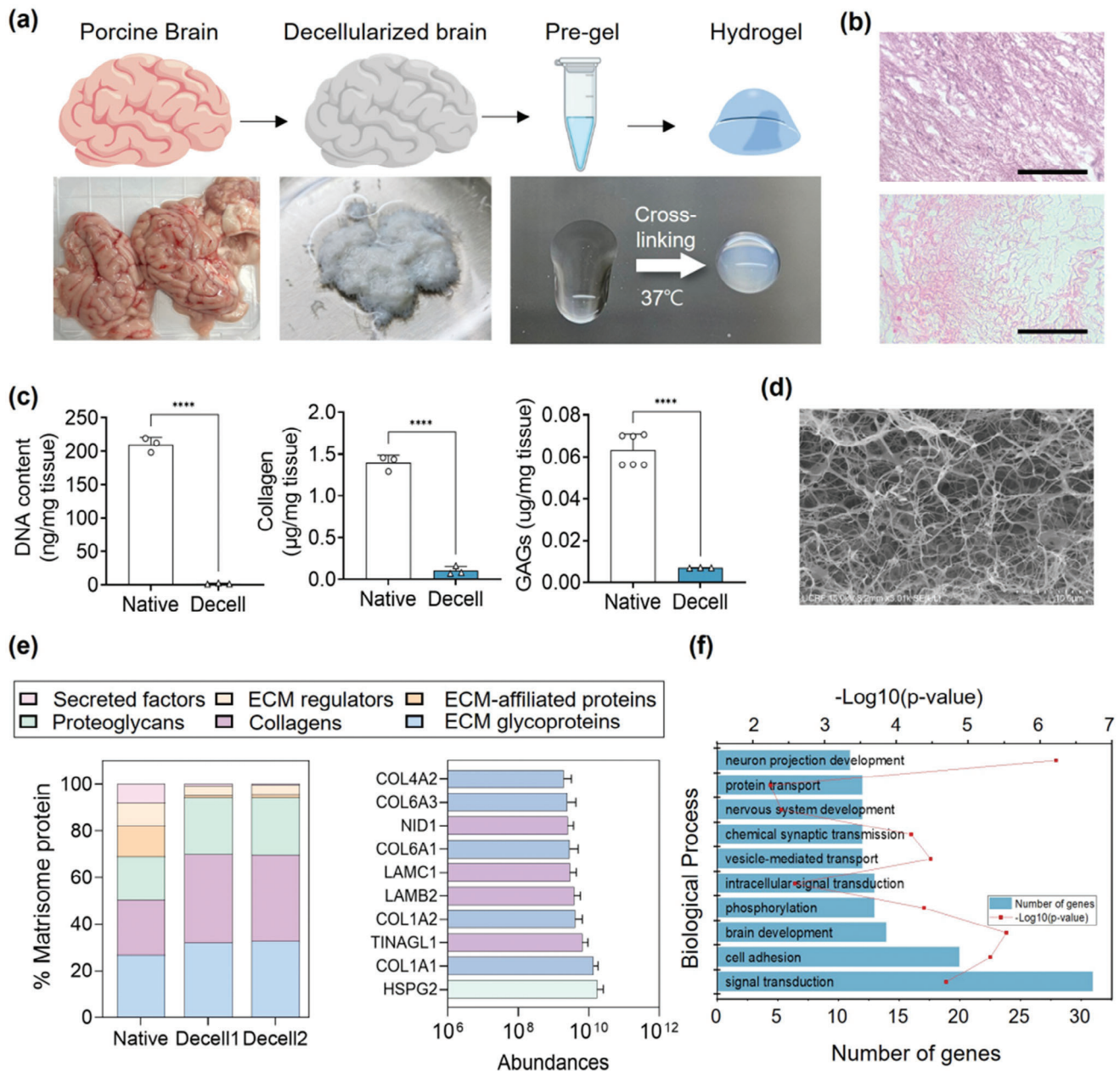


Figure 1. Characterization of brain-decellularized ECM (bdECM). a) Schematic representation of bdECM hydrogel formation for a 3D culture system of K562 adapted to the brain microenvironment. b) Hematoxylin and eosin (H&E) staining of the porcine brain before and after decellularization (scale bar = 100 µm). c) DNA, collagen, and glycosaminoglycans (GAGs) contents of porcine brain tissues before and after decellularization. d) Scanning electron microscopic observation that shows the internal ultrastructure of bdECM hydrogels (scale bars = 10 µm). e, f) Proteomic analysis of bdECM. e) Comparison of the composition of total matrisome proteins (left) and the top ten matrisome proteins with the highest expression (right) in two batches of bdECM; Decell1 and Decell2 (biological replicates = 2). f) The top 10 biological process terms ordered by number of genes after GO enrichment analysis of brain-enriched proteins exclusively present in bdECM. * $p < 0.05$, ** $p < 0.01$, *** $p < 0.001$, and **** $p < 0.0001$. ($n \geq 3$).

(KEGG) pathway analysis further indicated the potential role of bdECM in various physiological activities, highlighting its importance in fostering cell-matrix interactions. Upon comparing proteins known for at least fourfold higher expression in human brain tissue versus in other tissues by using data from the Human Protein Atlas (<https://www.proteinatlas.org/>), bdECM contained 202 such proteins. In contrast, Matrigel displayed only

four proteins (Figure S1c, Supporting Information). Furthermore, BP analysis of these 202 proteins in the bdECM indicated that they were involved in brain and nervous system development (Figure 1f). Overall, our proteomic analysis indicated that the protein composition of bdECM bears greater resemblance to human brain tissue than Matrigel, emphasizing its potential utility as a cellular scaffold for accurately mimicking the brain microen-

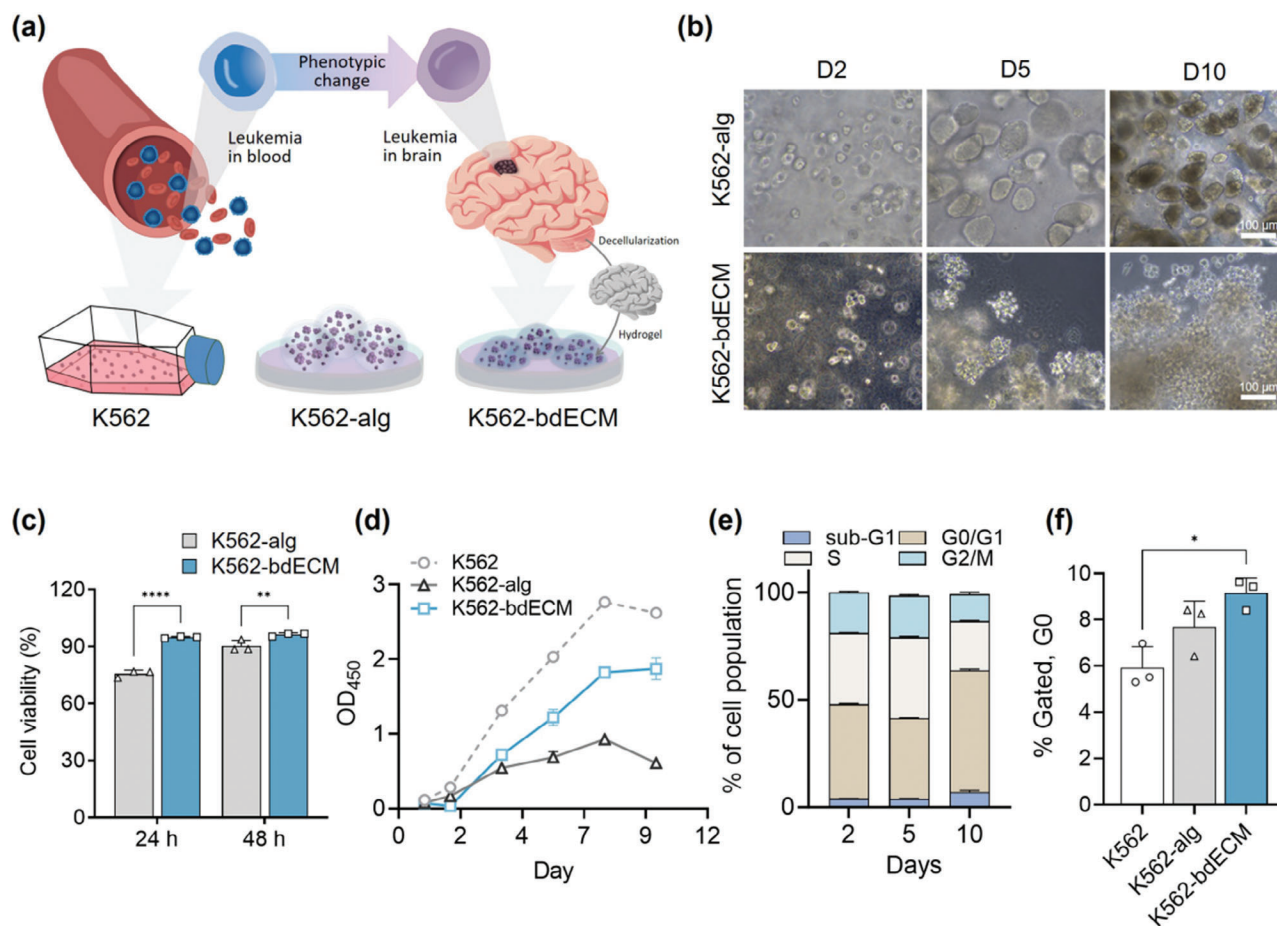


Figure 2. Characterization of engineered intracranial MS. a) Schematic diagram outlining the process for generating the intracranial MS model. b) Representative bright-field images of K562 cultured in 3D on brain dECM hydrogel or alginate hydrogel (named K562-bdECM and K562-alg, respectively). Scale bar = 100 μm. c) Assessment of cell viability through live/dead assay conducted at 24 and 48 h post-embedding in alginate or bdECM. d) Proliferation rate for K562 cultured by different days using WST-8 assay. e) Cell cycle profile with flow cytometry analysis for K562-bdECM on days 2, 5, and 10 of culture. f) G0 population on day 10 of culture through flow cytometry analysis for Pyronin Y staining. The number of repetitions for all quantitative data is 3 or more. * $p < 0.05$, ** $p < 0.01$, *** $p < 0.001$, and **** $p < 0.0001$. ($n \geq 3$).

environment. This is supported by numerous previous studies that demonstrated the ability of bdECM to emulate phenotypical cell behaviors in the brain more accurately than Matrigel.^[15] Consequently, we opted for the usage of bdECM over Matrigel to investigate the influence of bioactive brain ECM molecules on the structure of the MS tissue, which is a key interest of our research.

2.2. Alterations in the Cellular Phenotype of K562 Induced By Interaction With Brain ECM

During the blast crisis phase, CML cells circulate in the bloodstream and eventually migrate to the brain via complex mechanisms that are not yet fully understood.^[5] Once these cells enter the brain parenchyma, they begin to expand, leading to leukemic infiltration or formation of intracranial MS. However, the exact molecular mechanisms driving this process are not completely known. The phenotype of CML cells that expand into the brain can change in response to the surrounding microenvironment, potentially leading to the development of drug resistance.

To observe the CML cells that invaded the brain, we cultured K562 cells derived from patients with CML in the blast crisis phase within a 3D bdECM hydrogel (Figure 2a). We then investigated the phenotypic changes in K562 cells as they adapted to the brain ECM microenvironment. After 10 d of culture, we compared K562 cells grown in bdECM (K562-bdECM) with those embedded in alginate (K562-alg) devoid of biological motifs (Figure 2b and Figure S2a, Supporting Information). Unlike K562 cells in standard suspension cultures, 3D encapsulated K562 cells grew to form aggregates, similar to the MS tissue. K562-bdECM cells showed significantly higher initial survival rates at 24 and 48 h than K562-alg cells (Figure 2c and Figure S2b, Supporting Information), highlighting the importance of interaction with the ECM in the initial formation of intracranial MS. We noted the consistent proliferation of K562 cells in all experimental groups up to day 8, with cell viability remaining unchanged on day 10. At each time point examined, the viability of 3D-cultured K562 cells (both K562-bdECM and K562-alg) was lower than that of conventionally cultured K562 cells (K562). However, K562-bdECM had higher cell viability than K562-alg

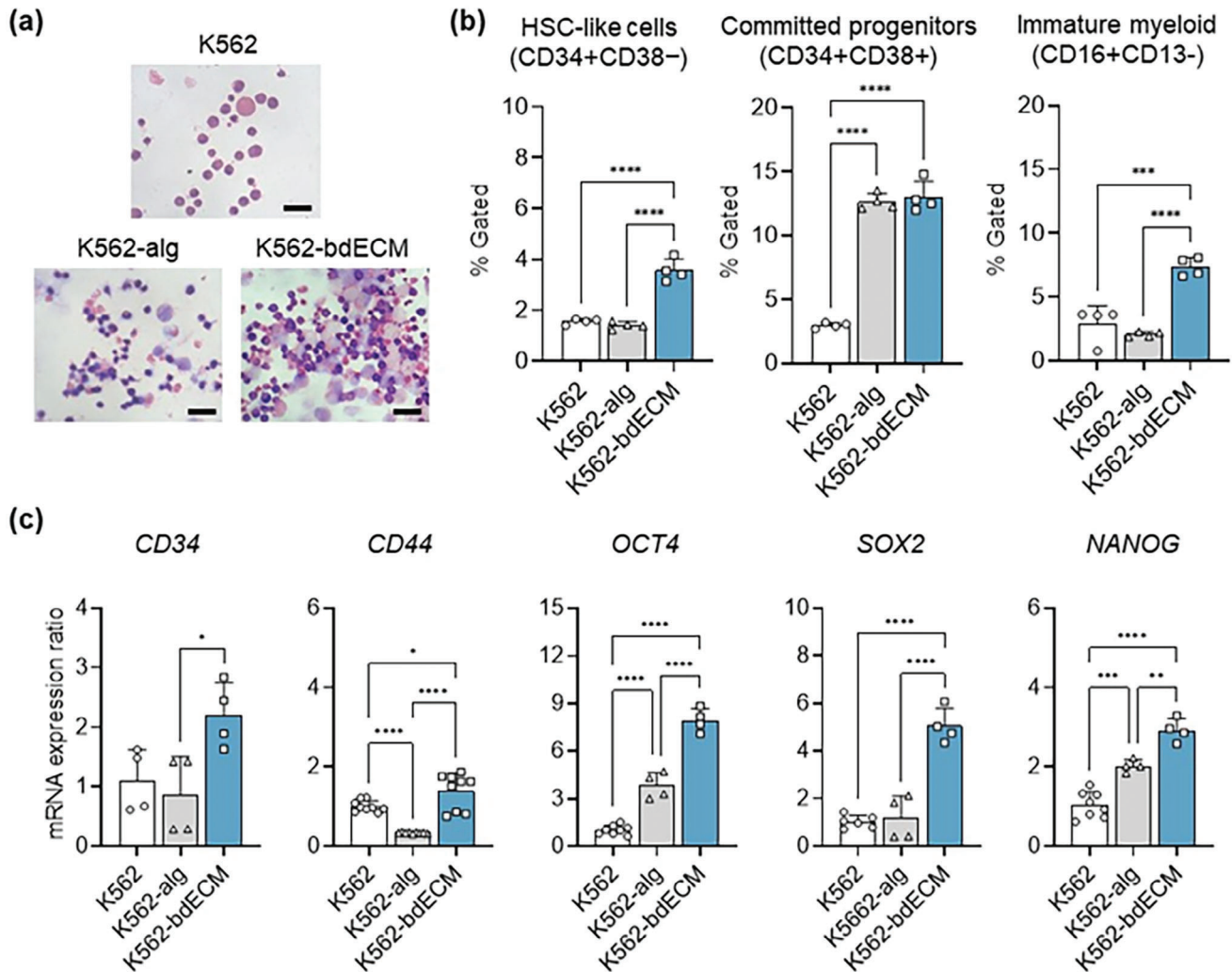


Figure 3. Differentiation pattern changes and leukemia stem cells expansion in K562 within engineered intracranial MS model. a) Representative images of Wright–Giemsa staining on K562 cultured in different platforms. Scale bar = 50 μ m. b) Flow cytometry analysis of K562 under various culture conditions, highlighting the presence of surface markers for leukemia stem cells and immature myeloid cells. c) The mRNA expression of genes encoding leukemia stem cells including *CD34*, *CD44*, *OCT4*, *SOX2*, and *NANOG*. The number of repetitions for all quantitative data is 3 or more. * $p < 0.05$, ** $p < 0.01$, *** $p < 0.001$, and **** $p < 0.0001$. ($n \geq 3$).

cells (Figure 2d). These observations align with those of previous studies, demonstrating that motifs and ligands within the ECM hydrogel enhance cell survival.^[16]

Subsequently, we explored changes in cell cycle distribution influenced by different culture conditions, as this provided insights into the proliferative status and response of CML cells to treatment. No significant changes were observed in the cell cycle distributions of K562-alg and K562 cells from days 2 to 10 (Figure S2c, Supporting Information). In contrast, K562-bdECM cells exhibited an increase in the G0/G1 phase and a decrease in the S and G2/M phases on day 10 (Figure 2e). More importantly, an increase in the population of G0 cells was observed, indicating a dormant phase,^[17] in K562-bdECM cells compared to both K562-alg and K562 cells, whereas this increase was only significant compared to that in K562 cells (Figure 2f). The G0 population of K562-bdECM rose from 43.3% on day 2 to 56.7% on day 10 (Figure S2d, Supporting Information). The increased percent-

age of dormant cells in the bdECM implies that a subset of MS cells in the brain may endure treatment with imatinib and other TKIs, given that these medications predominantly target actively proliferating cells. Furthermore, the presence of dormant cells may trigger stress-induced intracellular signaling, including the p38 MAPK pathway, which may play a role in the development of drug resistance.^[17]

We further evaluated changes in the maintenance of leukemia stem cells (LSCs) and proliferation of K562 cells within the brain microenvironment (Figure 3). K562 is a myeloid leukemia cell line derived from patients with blast crisis CML and is composed mostly of undifferentiated granulocytes and erythrocytes. Wright–Giemsa staining revealed that K562-bdECM displayed a wider range of cell shapes, indicating varied lineage differentiation in the brain ECM (Figure 3a). Through flow cytometry analysis, we observed a higher proportion of LSC (CD34⁺/CD38⁻ and CD34⁺/CD38⁺) and immature myeloid cells (CD16⁺/CD13⁻) in

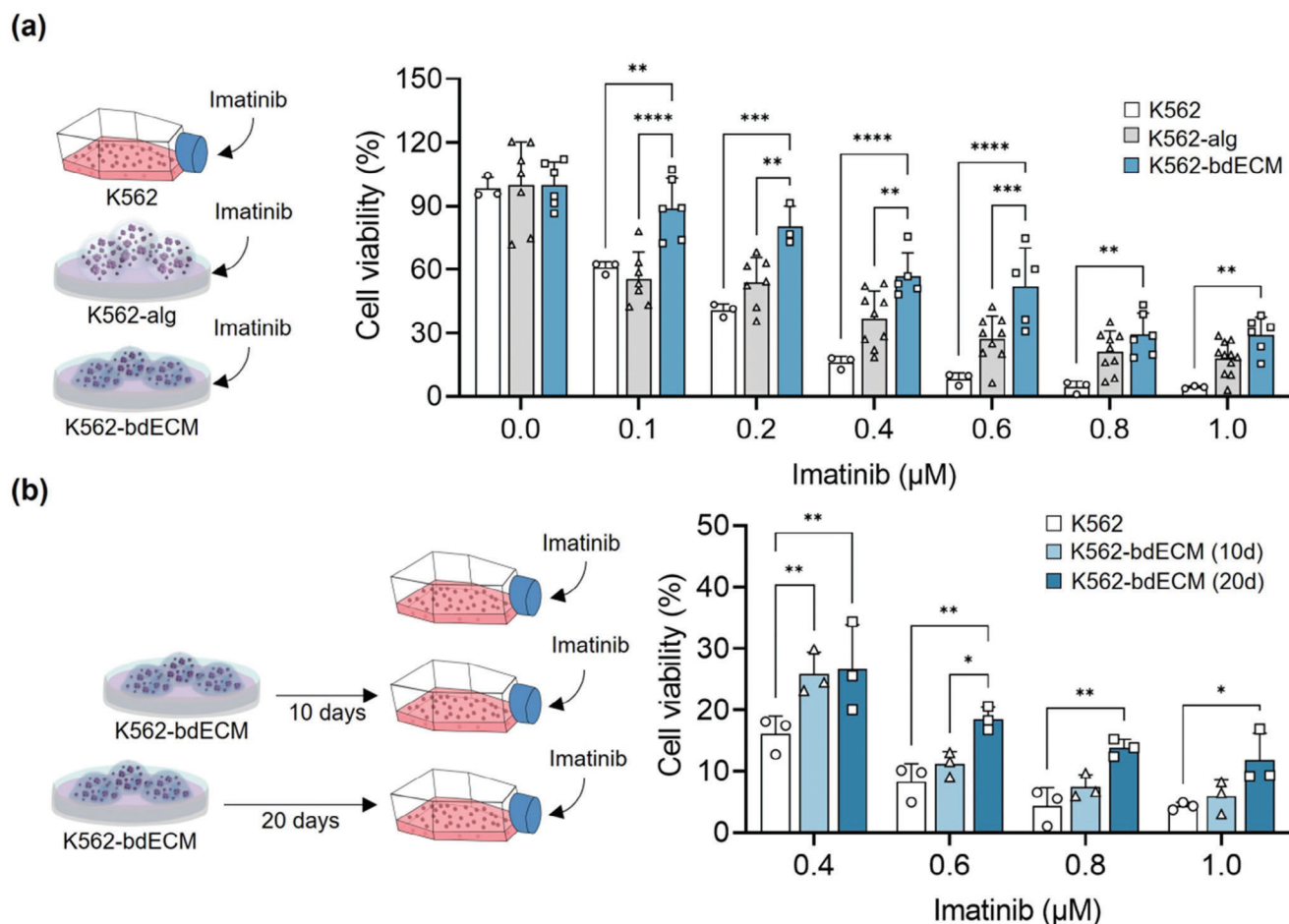


Figure 4. Sensitivity of K562 to imatinib in various culture conditions. a) Left: a scheme of the experimental design. Right: cell viability of K562 following treatment with imatinib in various concentrations measured by WST-8 assay. b) Left: a scheme of the experimental design. Right: cell viability of K562 extracted from bdECM after 10 and 20 days of 3D culture. The number of repetitions for all quantitative data is 3 or more. * $p < 0.05$, ** $p < 0.01$, *** $p < 0.001$, and **** $p < 0.0001$. ($n \geq 3$).

K562-bdECM than in K562 (Figure 3b), which has been observed in CML patients undergoing blast crisis compared to those in the chronic phase.^[18] In particular, the subpopulation of more primitive HSC-like LSCs ($CD34^+/CD38^-$) was approximately twofold higher in K562-bdECM than in K562 or K562-alg, which is consistent with the increase in dormant cells in K562-bdECM (Figures 3b and 2f). In patients with CML, the percentage of $CD34^+$ cells is typically greater in those undergoing blast crisis than in those in the chronic phase,^[18] suggesting that K562-bdECM more accurately mirrors the extramedullary blast crisis phase of CML. Additionally, quantitative polymerase chain reaction (qPCR) analysis showed significantly higher expression of LSC markers ($CD34$, $CD44$, $OCT4$, $SOX2$, and $NANOG$) in K562-bdECM than in standard K562 cells or K562 cells in alginate (Figure 3c).

Growing evidence supports that ECM components such as proteoglycans such as fibronectin, collagens (types I, IV, and VI), hyaluronan, and glycoproteins in the bone marrow are crucial for both healthy^[19] and LSCs,^[20] serving as a critical stem cell niche. The functions of the ECM include controlling cell adhesion and migration, proliferation and differentiation, and shape,

all of which are critical factors in stem cell niches.^[19] Our findings suggest that, similar to how LSCs interact with the bone marrow ECM to preserve their stem cell properties, the interaction of intracranial MS cells with brain ECM components may be crucial for maintaining LSC. This interaction could also be key to enabling these cells to enter a dormant state and survive outside the blood or bone marrow.

2.3. Acquisition of Imatinib-Resistant K562 by Interacting with Brain ECM

Our observation of phenotypic alterations in the cell cycle and stem cell expansion in K562-bdECM mimicked the extramedullary blast crisis in CML, which frequently demonstrates altered drug sensitivity levels.^[7] To investigate whether drug sensitivity could be replicated, K562-bdECM cells were treated with imatinib and their survival rate was assessed (Figure 4a). Notably, in all treatment groups, only K562-bdECM cells exhibited a significant increase in survival in response to imatinib. While K562-alg cells also displayed diminished drug sensitivity, the difference

was not statistically significant compared with the survival rate of conventionally cultured K562 cells, highlighting that the interaction of K562 cells with bdECM potentially fosters the emergence of drug resistance.

Subsequently, to rule out any errors that might arise from the differing rates of imatinib diffusion in conventionally cultured K562 cells (i.e., in suspension) and in K562-bdECM, K562 cells were removed from the bdECM hydrogel after 10 and 20 days of 3D culture. The cells were then exposed to imatinib in suspension culture. The data indicated an increased survival rate for K562-bdECM compared to K562 cells, with imatinib concentrations ranging from 0.4 to 1 μM (Figure 4b). Although an upward trend was observed in cell viability for K562 cells cultured in bdECM for 20 days compared to 10 days, the only significant change noted was when the cells were treated with imatinib at 0.6 μM . These data imply that interactions with the brain ECM microenvironment can lead to the development of drug resistance in K562 cells. Drug resistance is a significant hurdle in MS treatment strategies, making it crucial to understand the distinct characteristics of drug-resistant cells.

2.4. Adaptation of K562 to the Brain ECM Microenvironment Induces *ABCB1* Overexpression

To identify the underlying reasons for imatinib resistance observed in K562-bdECM, RNA sequencing was performed on K562, K562-bdECM, and K562-alg, all cultured for 10 days (Figure 5). This timeframe is when cell expansion halts and phenotypic changes become evident, based on our experimental results. Principal component analysis (PCA) indicated that although 3D-cultured K562 cells shared some similarities, the three groups were distinct (Figure 5a). Hierarchical clustering analysis demonstrated significant differential expression of 1158 genes between K562 and K562-bdECM cells, with 536 genes upregulated in the latter (Figure 5b). The upregulated genes in K562-bdECM were associated with various pathways, such as MAPK signaling, PI3K-Akt signaling, HIF-1 α signaling, autophagy, FoxO signaling, and ferroptosis as identified in KEGG analysis (Figure 5c). These pathways play pivotal roles in the proliferation, differentiation, and development of drug resistance in CML.^[21] In particular, the MAPK and PI3K-Akt signaling pathways have established connections with alterations in drug sensitivity in leukemia^[22] and have also been shown to influence the behavior of leukemic cells mediated by ECM proteins.^[23] Therefore, our MS model (K562-bdECM) demonstrated that the 3D interactions between leukemia cells and the surrounding bdECM can further stimulate signaling pathways associated with the development of drug resistance and mechanisms for evading cell death when compared to conventional culture methods using K562 cells alone. To better understand the observed drug resistance, we examined a subset of 234 genes associated with drug resistance through hierarchical clustering and identified genes that were significantly upregulated exclusively in K562-bdECM (Figure 5d).

Among these upregulated genes, *ABCB1* (ATP-binding cassette sub-family B member 1) encoding P-glycoprotein (P-gp), exhibits an ≈ 2.5 -fold upregulation in K562-bdECM compared to K562 and a 3.4-fold increase compared to K562-alg (Figure 5d and Figure S3a, Supporting Information). P-gp, a crucial reg-

ulator that facilitates the transport of drugs across cell membranes, reduces the intracellular drug concentration and its effectiveness. Overexpression or functional changes in *ABCB1* are often correlated with drug resistance, including imatinib resistance, which compromises the effectiveness of chemotherapy.^[24] *ABCB1* upregulation in K562-bdECM compared to that in K562 or K562-alg cells was further verified by qPCR and flow cytometry (Figures 5e,f). Moreover, to verify the functionality of the P-gp pump, we measured the accumulation of rhodamine 123, a P-gp substrate, and observed an increase in accumulation that correlated with the concentration of verapamil (a P-gp inhibitor) (Figure 5g), implying that P-gp is functional in K562-bdECM.

We further explored whether hypoxia was the principal factor driving the upregulation of *ABCB1* in K562-bdECM. To examine this, K562 cells were cultured in hypoxic environments with 5% O_2 and *ABCB1* levels were analyzed using qPCR (Figure S3b). Interestingly, the results indicated that hypoxia alone was not sufficient to augment *ABCB1* expression in K562 cells, suggesting that the upregulation of *ABCB1* may be attributed to the 3D interaction between K562 cells and their surrounding brain matrix. Similarly, in acute leukemia cells, previous studies utilizing 2D cultures^[23b,25] and in vivo mouse models^[26] have confirmed the development of drug resistance due to the upregulation of efflux pumps when exposed to ECM proteins. Collectively, our data suggest that the unique microenvironment provided by the brain ECM induces unique gene expression patterns and various molecular biological cell signaling pathways that may contribute to the development of drug resistance involving efflux pumps.

To determine whether the development of imatinib resistance in K562-bdECM (as shown in Figure 4) was associated with increased expression of *ABCB1*, we examined the impact of verapamil (a P-gp inhibitor) on imatinib sensitivity. Expectedly, the viability of K562-bdECM decreased in a concentration-dependent manner when exposed to 0.2 μM imatinib compared to the untreated group (Figure 5h). Conversely, treatment of K562-bdECM with MK571, an inhibitor of MRP1 (*ABCC1*), did not influence sensitivity to imatinib (Figure 5i). These results raise the possibility that the upregulated expression of P-gp plays a role in imatinib resistance in K562-bdECM.

2.5. Interaction of K562 with the Brain ECM May Promote Survival through Ferroptosis Suppression

We confirmed the drug resistance of K562-bdECM by observing the upregulation of the efflux pump P-gp (Figure 5). However, K562 cells exhibited resilience and survival even when exposed to a P-gp inhibitor, indicating an adaptation to their microenvironment in the brain ECM. This led us to explore the alterations in the cellular mechanisms that facilitate adaptation and survival during imatinib exposure. KEGG analysis of RNA-seq data suggested the upregulation of genes involved in the ferroptosis pathway, a regulated cell death mechanism characterized by iron-dependent lipid peroxide accumulation and resulting in cell membrane damage and subsequent cell death (Figure 5c). Notable differences were found between K562-bdECM and K562 cells, particularly in the gene set that inhibited ferroptosis, which included 204 relevant genes^[27] (Figure 6a and Figure S4, Supporting Information). Furthermore, we found that

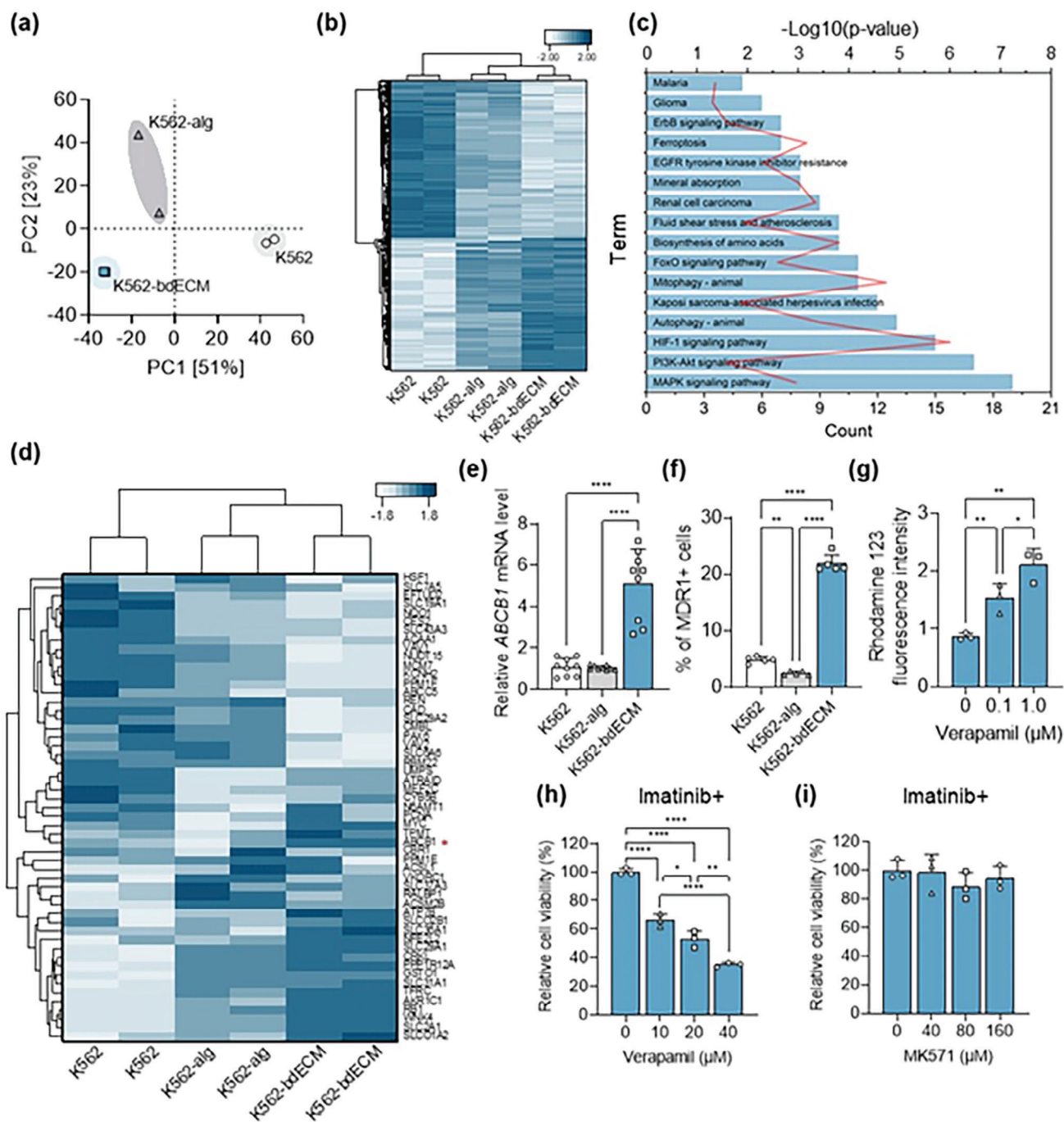


Figure 5. Bulk RNA-sequencing analysis of K562, K562-*alg*, and K562-*bdECM* and imatinib resistance of K562-*bdECM* related to upregulation of P-gp. a) A PCA plot of K562 in various culture conditions. b) Heatmap clustering genes exhibiting at least a twofold difference in expression compared to those in K562 based on Euclidean distance. c) KEGG functional classification showcases genes that are upregulated in K562-*bdECM* when compared to K562. d) A heatmap clustering data for 234 drug resistance-associated genes, with the comparison set among K562, K562-*bdECM*, and K562-*alg* based on Euclidean distance. An asterisk indicates differential expression of *ABCB1*. e) The mRNA expression ratio of *ABCB1* gene in the K562-*alg* and K562-*bdECM* relative to K562 analyzed by qPCR. f) Flow cytometry analysis of K562 cells expressing *ABCB1*/P-gp protein. g) Evaluation of cellular internalization of rhodamine 123 as a substrate of P-gp in the presence of verapamil (a P-gp inhibitor). h) Viability of K562-*bdECM* upon 0.2 μM imatinib exposure in the presence of verapamil, measured using a WST-8 assay. i) Viability of K562-*bdECM* upon 0.2 μM imatinib exposure in the presence of MK571, an MRP1 inhibitor, measured using a WST-8 assay. The number of repetitions for all quantitative data is 3 or more. **p* < 0.05, ***p* < 0.01, ****p* < 0.001, and *****p* < 0.0001. (*n* ≥ 3).

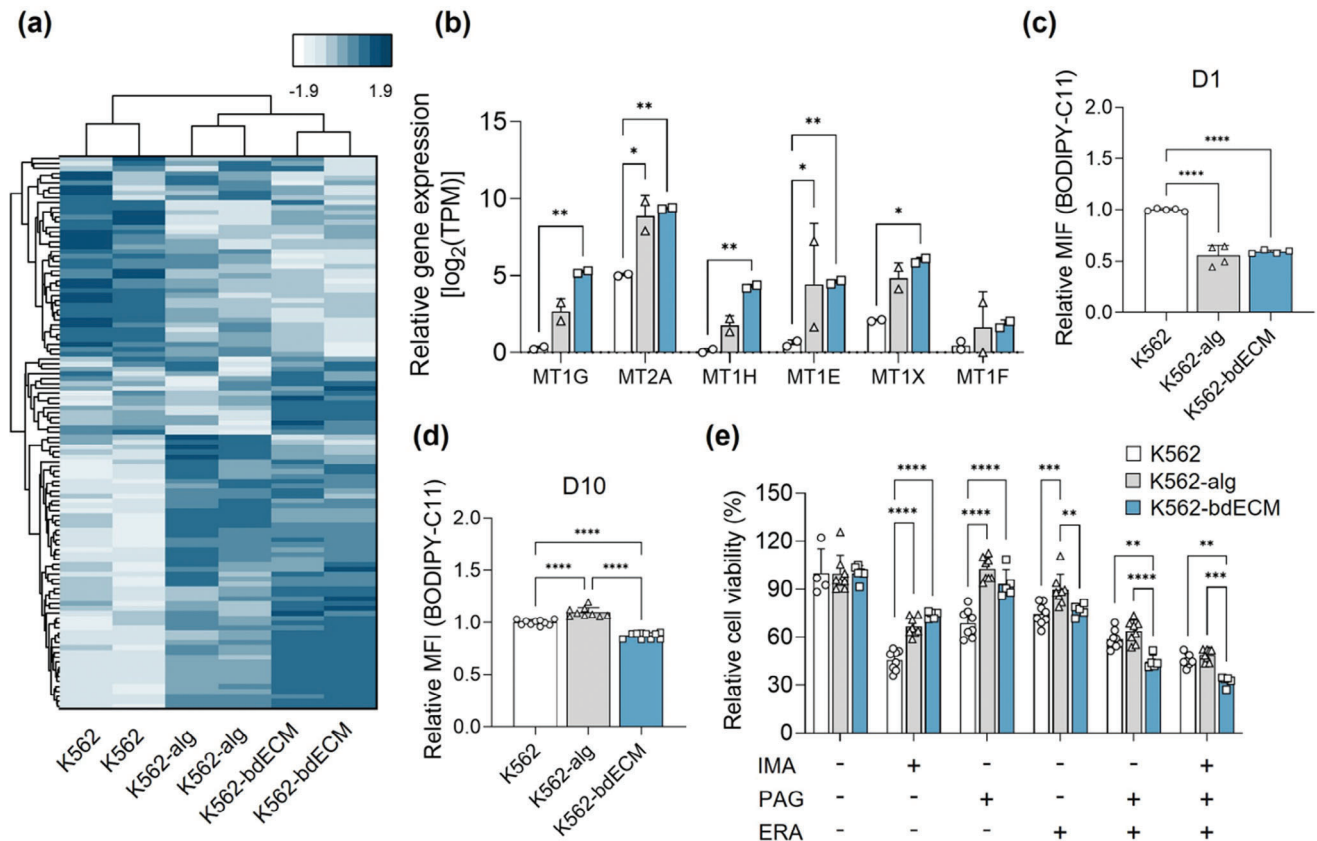


Figure 6. Suppression of ferroptosis in K562-bdECM. a) A heatmap clustering data for ferroptosis suppressor genes, with the comparison set among K562, K562-bdECM, and K562-alg based on Euclidean distance. b) Normalized gene expressed levels (TPM; transcript per million) from RNA-seq data for genes encoding metallothionein proteins. c,d) Flow cytometry analysis shows K562 cells stained with BODIPY-C11 (a ferroptosis indicator) on days 1 (c) and 10 (d) of culture. Depicted is the relative mean fluorescence intensity (MFI) of BODIPY-C11 in K562-alg and K562-bdECM, compared to K562. e) Viability of K562, K562-alg, and K562-bdECM in the presence of various compounds: 2 mM propargylglycine (PAG; an inhibitor of ferroptosis suppressor metallothionein), 5 μM Erastin (ERA; a ferroptosis inducer), and 0.2 μM imatinib (IMA).

metallothionein genes (e.g., *MT1G*, *MT2A*, *MT1H*, *MT1E*, and *MT1X*) were highly elevated in K562-bdECM, which are known to indirectly suppress the initiation of ferroptosis by binding to iron^[28] (Figure 6b). This suggests that interactions with the brain ECM may enhance the survival of patients with MS by obstructing ferroptosis. Many cancer types downregulate the ferroptosis pathway to diminish their sensitivity, consequently developing resistance to cancer treatment.^[29] While research on ferroptosis in CML is limited, emerging evidence indicates the potential of promoting ferroptosis as a therapeutic strategy for acute leukemia.^[30] These data support our hypothesis that the ECM microenvironment of the brain may suppress ferroptosis.

To test this possibility, we assessed the ferroptosis levels in K562 cultures by measuring lipid peroxidation using C11-BODIPY staining^[31] (Figure 6c,d). On day one of culture, a notably lower induction of ferroptosis was observed in 3D-cultured K562-bdECM and K562-alg cells than in K562 (Figure 6c). By day 10, although K562-alg exhibited a recovery in its ferroptosis level, K562-bdECM maintained a significantly reduced level compared to K562; this aligns with the insights from our RNA-seq data (Figure 6d). Furthermore, we subjected K562, K562-alg, and K562-bdECM cells to ERA (which is known to induce

ferroptosis)^[27] or a combination with PAG (which downregulates metallothionein)^[30a,32] to determine whether promoting drug-led ferroptosis might offer promise in treating MS. The WST-8 assay indicated that ERA-induced ferroptosis slightly reduced the survival of K562-bdECM cells, a response markedly amplified by PAG (Figure 6e). This suggests that inhibiting metallothionein, which is upregulated in the brain ECM microenvironment, can intensify ferroptosis induction. Remarkably, co-treatment with PAG and ERA affected the viability of K562-bdECM cells more than treatment with K562 or K562-alg alone. A similar pattern emerged with a 0.2 μM dose of imatinib, showing higher sensitivity compared to K562 or K562-alg (Figure 6e). These results indicate the potential of targeting MS cells acclimatized to the brain ECM through ferroptosis to overcome drug resistance.

3. Conclusion

In our study, we observed distinct phenotypic alterations in suspension leukemia cells when they formed a tumor-like mass in the brain by developing the first intracranial MS model based on decellularization technology. By contrasting K562-bdECM with K562-alg through several biological and physiological evalu-

ations, we found that the adaptive shift of K562 in the brain ECM microenvironment (marked by changes in the cell cycle, stem cell populations, increased *ABCB1* expression, and ferroptosis suppression) may lead to the drug resistance observed in patients with MS. Interestingly, our findings indicate that combating ferroptosis promotion could offer a novel approach to address the challenges of treating intracranial MS. Overall, our research suggests that the intracranial MS model can serve as an efficient and robust tool for examining phenotypic changes as cells adapt to their microenvironment and for rapidly assessing anticancer drugs against which cells may develop resistance.

Nonetheless, a deeper understanding of these phenotypic shifts requires further studies to elucidate the molecular mechanisms of cell evasion and adaptation. Comprehensive studies, such as animal-based experiments for intracranial MS or validation using patient samples, are crucial for ascertaining the reliability and effectiveness of our simplified culture model. Moreover, enriching the cellular complexity of the intracranial MS model would provide insights into the effects of the interactions with brain cells.

4. Experimental Section

Decellularization of PORCINE Brain Tissue: Decellularization of the brain tissue was performed as previously described^[33] with slight modifications. Fresh porcine brain (Sanggae-ro, Meat Distribution in Ulsan, Republic of Korea) was immediately frozen at -80°C . Brain tissue was chopped into small pieces ($\approx 0.8 \times 0.8 \times 0.8 \text{ cm}^3$). For the initial wash, the chopped brain tissue was agitated in 5 L of distilled water for 24 h at 4°C . The used washing liquid was subsequently decanted through a $254\text{-}\mu\text{m}$ stainless steel mesh, ensuring retention of the brain tissue. Following this step, the remaining tissue was agitated sequentially in various buffer solutions: 0.02% trypsin (WELGENE, Republic of Korea) for 2 h, 3% Triton X-100 (LPS solution, Daejeon, Republic of Korea) for 1 h, 1.0 M sucrose (DaeJung Chemicals, Republic of Korea) for 20 min, 4% sodium deoxycholate (Sigma-Aldrich, USA) for 60 min, and 4% ethanol (Merck, USA). Following these steps, the decellularized brain tissue was sterilized using a 1% antibiotic solution (penicillin/streptomycin, P/S, WELGENE, Republic of Korea) for an additional 24 h. Each solution was completely removed, and the tissue was rinsed with distilled water between each step. All the procedures were performed at room temperature (RT). Once sterilized, the dECM was lyophilized and stored at -80°C until needed.

To prepare the bdECM solution, the lyophilized ECM was resuspended in a 0.01 N HCl solution at a concentration of 10 mg mL^{-1} and digested with 1 mg mL^{-1} pepsin for 48 h at RT. Following digestion, undigested residues were filtered out through a $100\text{-}\mu\text{m}$ strainer (SPL Life Sciences, Republic of Korea). The resulting digest was then neutralized to a pH of 7.2–7.5 using 10x phosphate-buffered saline and 0.1 M NaOH solution at 4°C . The prepared 10 mg mL^{-1} pre-gel solution was cryopreserved at -20°C until use in future experiments. To form the final bdECM-based hydrogel, bdECM solution was incubated at 37°C for 30 min.

Characterization of bdECM: Scanning electron microscopy (SEM) imaging was performed to visualize the microstructure of the bdECM hydrogel after thermal gelation. To observe the cross-sections of the hydrogels, they were cut to expose their cross-sections and coated with platinum using a sputter coater (Hitachi E-1045, Japan). The sample surfaces and cross-sections were observed using SEM (Hitachi Model S-4800, Japan).

To quantify the amount of DNA remaining in native brain tissue and bdECM, DNA was extracted using an AccuPrep Genomic DNA extraction kit (Bioneer, Republic of Korea). The concentration of the DNA was measured using a NanoDrop One spectrophotometer (Thermo Fisher Scientific, USA) at 260 nm. The total hydroxyproline content of both the native tissue and bdECM was quantified using a hydroxyproline assay kit

(Biomax, Republic of Korea). The glycosaminoglycan (GAG) content was measured using a dimethylmethylene blue (DMMB) assay kit (Blyscan, USA). All assay kits were used in accordance with the manufacturers' guidelines.

For histological evaluation, the samples were fixed with a 4% paraformaldehyde solution and embedded in paraffin. Tissue sections ($10 \mu\text{m}$) were stained with H&E following standard procedures.

For mechanical analysis, the 10 mg mL^{-1} bdECM hydrogel was tested at a rate of 1 mm min^{-1} on an Instron 3343 mechanical analyzer (Instron, Canton, USA). The compressive modulus was calculated from the slope of the stress–strain curve in the linear region.

LC–MS/MS Analysis and Proteome Data Analysis: E-biogen (E-biogen, Inc., South Korea) was used for the proteomic analyses. The protein concentration was determined using the Pierce BCA protein assay kit (Thermo Fisher Scientific). The digestion process was performed using filter-aided sample preparation on a Microcon 30K centrifugal filter (Millipore, USA). Samples were first reduced by incubation with tris (2-carboxyethyl)phosphine at 37°C for 30 min, followed by alkylation with iodoacetic acid (IAA) at 25°C for 1 h in the dark. After sequential washing with lysis buffer and 50 mM ammonium bicarbonate, proteins were digested with trypsin (with a 1:50 enzyme to protein ratio, w/w) at 37°C for 18 h. Resulting peptides were transferred to new tubes and trypsin was inactivated by adding $14 \mu\text{L}$ of formic acid (Honeywell, USA). The peptides were then desalted using C18 spin columns (Harvard Apparatus, USA), and elution was achieved using 80% acetonitrile in 0.1% formic acid in water.

The prepared samples were resuspended in 0.1% formic acid in water and analyzed using a Q-Exactive Orbitrap hybrid mass spectrometer (Thermo Fisher Scientific) and an Ultimate 3000 system (Thermo Fisher Scientific). We used a $2 \text{ cm} \times 75 \mu\text{m}$ ID trap column packed with $3\text{-}\mu\text{m}$ C18 resin and a $50 \text{ cm} \times 75 \mu\text{m}$ ID analytical column packed with $2\text{-}\mu\text{m}$ C18 resin to peptides depending on peptide hydrophobicity. The mobile phase solvent consisted of A) 0.1% formic acid in water and B) 0.1% formic acid in 90% acetonitrile, and the flow rate was fixed at 300 nL min^{-1} . The mobile phase gradient was as follows: 4% solvent B for 14 min, 4–15% solvent B for 61 min, 15–28% solvent B for 50 min, 28–40% solvent B for 20 min, 40–96% solvent B for 2 min, holding at 96% solvent B for 13 min, 96–4% solvent B for 1 min, and 4% solvent B for 24 min. A data-dependent acquisition method was adopted, and the top ten precursor peaks were selected and isolated for fragmentation. Ions were scanned at high resolution (70 000 in MS1, 17 500 in MS2 at m/z 400), and the MS scan range was 400–2000 m/z at both the MS1 and MS2 levels. The precursor ions were fragmented with a normalized collisional energy of 27%. Dynamic exclusion was set at 30 s.

Thermo MS/MS raw files of each analysis were searched by using Proteome Discoverer software (ver. 2.5) and the Sus scrofa database was downloaded from UniProt. The appropriate consensus workflow included a peptide-spectrum match validation step and the SEQUEST HT process for detection as a database search algorithm. The search parameters were set as follows: 10 ppm tolerance of precursor ion masses, 0.02 Da fragment ion mass, and a maximum of two missed cleavages with trypsin. After searching, data results below 1% false discovery rate were selected and filtered for at least six additional peptides. Mass spectrometry proteomics data were deposited in the ProteomeXchange Consortium via the PRIDE^[34] partner repository with the dataset identifier PXD047117.

Reconstitution of Intracranial MS Using bdECM: Human leukemic K562 cells were purchased from Korean Cell Line Bank (Republic of Korea). Cells were cultured in a RPMI 1640 growth medium (GM; WELGENE, Republic of Korea) supplemented with 10% (v/v) fetal bovine serum and 1% (v/v) penicillin/streptomycin. The K562 cell suspension at a concentration of $1 \times 10^6 \text{ cells mL}^{-1}$ was mixed in a 1:1 ratio with bdECM or alginate solution at a concentration of 10 mg mL^{-1} . Finally, droplets of the cell/bdECM mixture containing $5 \times 10^5 \text{ cells mL}^{-1}$ of K562 and 5 mg mL^{-1} of bdECM solution were placed in a 48-well plate and solidified in an incubator set at 37°C for 30 min. A droplet of the cell-alginate mixture was solidified in a solution of 100 mM calcium chloride in 10 mM HEPES-buffered saline at RT for 10 min and washed twice with GM. Encapsulated K562 cells were cultured at 37°C in a fully humidified 5% CO_2 incubator.

Cell Viability and Proliferation Assays: The viability of the encapsulated cells was evaluated using a viability/cytotoxicity kit (Invitrogen), following the manufacturer's protocol. Live (calcein-AM, green) and dead cells (ethidiumhomodimer-1, red) cells were detected using a fluorescence microscope (Nikon ECLIPSE Ts2, Tokyo, Japan). The obtained images were quantified using ImageJ software (National Institute of Health, USA).

The effect of 3D culture on cellular proliferation was measured using water-soluble tetrazolium salt WST-8 (Quanti-Max WST-8 Cell Viability Assay Kit, Biomax, Republic of Korea). Cells encapsulated in both the bdECM hydrogel and alginate gel were additionally incubated for 2 h with 10% WST-8 reagent at each determined time point. The absorbance of each well was recorded at 450 nm using a microplate reader (BioTek). The cell proliferation rate was calculated relative to that on day 1.

The sensitivity of encapsulated K562 cells to imatinib mesylate (Sigma–Aldrich) was determined using WST-8. After 24 h of encapsulation, the cells were treated with imatinib and further incubated for 48 h. The absorbance was measured at 450 nm using a microplate reader (BioTek). To evaluate anti-leukemia through ferroptosis induction, Erastin (ERA, 5 μM) (a known ferroptosis inducer) and Propargylglycine (PAG, 2 mM)^[30a] (which reduces metallothionein induction) were pretreated for 24 h before adding imatinib.

Activity of P-gp Efflux Pump Transporter: The P-glycoprotein efflux pump activity of K562-bdECM was assessed by monitoring the uptake of the glycoprotein substrate rhodamine 123 (Sigma–Aldrich). After 24 h of encapsulation, the cells were treated with verapamil (Sigma–Aldrich) for 3 h and washed twice with Dulbecco's phosphate-buffered saline (DPBS) twice. Subsequently, GM containing rhodamine 123 (300 ng mL^{-1}) was added, followed by incubation for 60 min. The medium containing rhodamine 123 was then removed and GM was added for an additional 60 min of incubation. Finally, K562 cells were washed twice with DPBS. The encapsulated cells were sonicated for 5 s to release rhodamine 123. The excitation/emission values were determined using a microplate reader at 485/590 nm.

QuantSeq 3' mRNA-Seq Analysis: QuantSeq was performed in duplicate (E-Biogen) on each group, and the data were analyzed using ExDEGA software (v4.0.3, E-Biogen). For control and test RNAs, the construction of the library was performed using QuantSeq 3' mRNA-Seq library prep kit (Lexogen, Austria), according to the manufacturer's instructions. In brief, each 500 ng total RNA were prepared and an oligo-dT primer containing an Illumina-compatible sequence at its 5'-end was hybridized to the RNA and reverse transcription was performed. After degradation of the RNA template, second strand synthesis was initiated by a random primer containing an Illumina-compatible linker sequence at its 5'-end. The double-stranded library was purified using magnetic beads to remove all reaction components. The library was amplified to add complete adapter sequences required for cluster generation. The finished library is purified from PCR components. High-throughput single-end 75 sequencing was performed using NextSeq 500 (Illumina, USA).

QuantSeq 3' mRNA-seq reads were aligned using Bowtie2.^[35] Bowtie2 indices were generated either from the genome assembly sequence or representative transcript sequences for alignment to the genome and transcriptome. The alignment file was used to assemble transcripts, estimate their abundance, and detect differential gene expression. Differentially expressed genes were determined based on counts from unique and multiple alignments using Bedtools.^[36] The read count data were processed based on the TMM + CPM normalization method using EdgeR within R (R Development Core Team, 2020) and using Bioconductor.^[37]

Flow Cytometry: For the cell cycle analysis, each group of cells (2×10^5 cells mL^{-1}) were double-stained with Pyronin Y/Hoechs33342 solution (100 μL of GM containing 4 $\mu\text{g mL}^{-1}$ of Pyronin Y and 10 $\mu\text{g mL}^{-1}$ of Hoechs33342) (Invitrogen) for 20 min in the dark at 37 °C. The cells were then resuspended in 200 μL GM and immediately analyzed by using a flow cytometer (BD FACS Verse with software BD FACSuite™, USA). The cell cycle distribution was analyzed using FCSalyzer (ver. 0.9.22-alpha) (<https://sourceforge.net/projects/fcsalyzer/>).

To analyze the expression of cell surface markers (e.g., CD13, CD16, CD34, CD38, and MDR1), cells were harvested and incubated with directly-labeled anti-human primary antibodies. The levels of cell surface marker

proteins were analyzed by a flow cytometer (BD FACS Verse with software BD FACSuite). The percentage of cell surface markers was analyzed using FCSalyzer.

To detect ferroptosis by using C11-BODIPY (581/591) (Thermo Fisher Scientific) staining, which measures lipid peroxide production, harvested K562 cells (2×10^5 cells mL^{-1}) were incubated with C11-BODIPY for 10 min at 37 °C in the dark. The cells were then washed twice and resuspended in 200 μL of fresh DPBS. Flow cytometry data were collected using FCSalyzer.

Quantitative PCR Analysis: Total RNA was extracted from cells cultured in different hydrogels using TRIzol reagent (Invitrogen). The RNA concentration was quantified using a Nanodrop One spectrophotometer (Thermo Fisher Scientific). The extracted RNA (500 ng) was converted to cDNA using AccuPower RocketScript RT PreMix (Bioneer, Republic of Korea). qPCR was conducted by using SYBR® Green Realtime PCR Master Mix (TOYOBO, Japan). Relative quantification of target genes was performed using the $2^{-\Delta\Delta\text{CT}}$ method. First, the target gene in each sample was normalized to RPS27 as a reference gene using threshold cycle information. The relative fold changes in gene expression in the target and negative control samples (K562 in suspension) were further analyzed. The primers used in this study are listed in Table S2.

Immunofluorescence: Cells were fixed with 4% paraformaldehyde and permeabilized with 0.2% Triton X-100 (Sigma–Aldrich) in DPBS. The cells were then treated with 3% bovine serum albumin (Sigma–Aldrich) in DPBS with 0.1% Triton X-100 for 1 h at RT to block the non-specific binding of antibodies. The cells were incubated with MRD1 primary antibody (Bioss Antibodies, USA) at 4 °C for 16 h, then with the secondary antibody conjugated with Alexa Fluor 488 and 594 (Invitrogen). Nuclei were stained with Hoechst 33342. Confocal imaging was performed using a Zeiss LSM 980 confocal laser scanning microscope and analyzed using Zeiss Zen Blue software.

Statistical Analysis: All quantitative data are expressed as the mean \pm standard deviation. Statistical analyses were performed using *t*-tests to compare two sets of data. One-way analysis of variance was used to compare multiple groups with Tukey's post hoc test using GraphPad Prism software (version 8, Graph Pad Software, Inc., San Diego, CA, USA; **p* < 0.05; ***p* \leq 0.01; ****p* \leq 0.001, and *****p* \leq 0.0001).

Supporting Information

Supporting Information is available from the Wiley Online Library or from the author.

Acknowledgements

This study was supported by a National Research Foundation of Korea (NRF) grant funded by the Ministry of Science and ICT (NRF-2021R1A4A3030597, 2022M3A91015716, 2020R1C1C1014753, and 2020M3A9B6038845), a Research Fund (1.240006.01) of Ulsan National Institute of Science and Technology.

Conflict of Interest

The authors declare no conflict of interest.

Author Contributions

H.Y. participated in the design and performance of all experiments and analyzed the data. J.H.K., S.W.C., and C.G.P. provided scientific supervision on hydrogel fabrication. T.E.P. and D.W.K. supervised all work.

Data Availability Statement

The raw reads were deposited into European Nucleotide Archive database and can be accessed via accession number PRJEB67695. The mass spectrometry proteomics data have been deposited to the ProteomeXchange

Consortium via the PRIDE 27 partner repository with the dataset identifier PXD047117.

Keywords

3D culture, brain-decellularized ECM, drug resistance, ferroptosis, leukemia, myeloid sarcoma

Received: December 9, 2023

Revised: January 31, 2024

Published online: February 13, 2024

- [1] a) Y.-C. Hsieh, K. Kirschner, M. Copland, *Leukemia* **2021**, *35*, 1229; b) V. R. Minciacci, R. Kumar, D. S. Krause, *Cells* **2021**, *10*, 117.
- [2] A. E. G. Osman, M. W. Deininger, *Blood Rev.* **2021**, *49*, 100825.
- [3] S. A. Pileri, S. Ascani, M. C. Cox, C. Campidelli, F. Bacci, M. Piccioli, P. P. Piccaluga, C. Agostinelli, S. Asioli, D. Novero, M. Bisceglia, M. Ponzoni, A. Gentile, P. Rinaldi, V. Franco, D. Vincelli, A. P. Jr, R. Gasbarra, B. Falini, P. L. Zinzani, M. Baccarani, *Leukemia* **2007**, *21*, 340.
- [4] a) S. Tsukamoto, S. Ota, C. Ohwada, Y. Takeda, M. Takeuchi, E. Sakaida, N. Shimizu, K. Yokote, T. Iseki, C. Nakaseko, *Leuk Res Rep* **2013**, *2*, 67; b) A. E. Whiteley, T. T. Price, G. Cantelli, D. A. Sipkins, *Nat Rev Cancer* **2021**, *21*, 461.
- [5] a) M. Jin, C. Xuan, J. Gao, R. Han, S. Xu, L. Wang, Y. Wang, K. Shi, S. Rauniyar, Q. An, *Medicine* **2018**, *97*, e13131; b) N. A. Johnson, R. Fetni, S. N. Caplan, *Leuk Lymphoma* **2005**, *46*, 629; c) P. K. Kiran, G. V. Badarke, C. N. Suresh, B. J. Srinivas, R. Naik, *South Asian J Cancer* **2018**, *7*, 170; d) K.-W. Lee, M.-K. Song, Y.-M. Seol, Y.-J. Choi, H.-J. Shin, J.-S. Chung, G.-J. Cho, *Korean J. Med.* **2009**, *77*, 441; e) L. A. B. Morillo, F. Zapata-Mesina, M. R. I. D. Castillo, *Int. Blood Res. Rev.* **2015**, *4*, 1; f) K. Oshima, Y. Kanda, T. Yamashita, S. Takahashi, T. Mori, C. Nakaseko, K. Fujimaki, A. Yokota, S. Fujisawa, T. Matsushima, H. Fujita, T. Sakura, S. Okamoto, A. Maruta, H. Sakamaki, *Biol Blood Marrow Transplant* **2008**, *14*, 1100; g) A. H. Palejwala, K. P. O'Connor, H. Shi, L. Villeneuve, T. Scordino, C. A. Glenn, *J Clin Neurosci* **2019**, *64*, 269; h) H. J. Kim, C. W. Jung, K. Kim, J. S. Ahn, W. S. Kim, K. Park, Y. H. Ko, W. K. Kang, K. Park, *J. Clin. Oncol.* **2006**, *24*, 4028; i) J. Arumugam, B. Karthik Bommanna, J. Kalaiyarasi, S. Sundersingh, *Indian J Med Paediatr Oncol* **2021**, *41*, 781; j) H. Boudiaf, K. Ezziane, N. O. Rouis, M. Himrane, S. Hakem, H. Benchabane, H. Boukhalal, R. Arous, L. Chikhi, *Pan Afr. Med. J.* **2020**, *36*, 142.
- [6] M. Łazarczyk, M. E. Mickael, D. Skiba, E. Kurzejamska, M. Ławiński, J. O. Horbańczuk, J. Radziszewski, K. Fraczek, R. Wolinska, J. Paszkiewicz, P. Religa, M. Sacharczuk, *Int. J. Mol. Sci.* **2023**, *24*, 3854.
- [7] a) P. Aftimos, F. Nasr, *Leuk Res* **2009**, *33*, e178; b) Y. Isobe, K. Sugimoto, A. Masuda, Y. Hamano, K. Oshimi, *Intern Med J* **2009**, *39*, 408; c) S. G. Papageorgiou, V. Pappa, C. Economopoulou, P. Tsigotis, F. Konsiotsi, E.-D. Ionnidou, S. Chondropoulos, D. Vasilatou, E. Papageorgiou, T. Economopoulos, J. Dervenoulas, *Leuk Res* **2010**, *34*, e254.
- [8] a) D. Deak, N. Gorcea-Andronic, V. Sas, P. Teodorescu, C. Constantinescu, S. Iluta, S. Pasca, I. Hotea, C. Turcas, V. Moisiu, A. A. Zimta, S. Galdean, J. Steinheber, I. Rus, S. Rauch, C. Richlitzki, R. Munteanu, A. Jurj, B. Petrushev, C. Selicean, M. Marian, O. Soritau, A. Andries, A. Roman, D. Dima, A. Tanase, O. Sigurjonsson, C. Tomuleasa, *Ann. Transl. Med.* **2021**, *9*, 68; b) K. E. Zorn, A. M. Cunningham, A. E. Meyer, K. S. Carlson, S. Rao, *Cancers* **2023**, *15*.
- [9] M. E. Gorre, M. Mohammed, K. Ellwood, N. Hsu, R. Paquette, P. N. Rao, C. L. Sawyers, *Science* **2001**, *293*, 876.
- [10] a) M. Karimpoor, E. Yebra-Fernandez, M. Parhizkar, M. Orlu, D. Craig, J. S. Khorashad, M. Edirisinghe, *J R Soc Interface* **2018**, *15*, 20170928; b) T. Harada, I. Tsuboi, M. Utsunomiya, M. Yasuda, S. Aizawa, *J. Biosci. Bioeng.* **2020**, *130*, 650.
- [11] a) X. Tian, M. E. Werner, K. C. Roche, A. D. Hanson, H. P. Foote, S. K. Yu, S. B. Warner, J. A. Copp, H. Lara, E. L. Wauthier, J. M. Caster, L. E. Herring, L. Zhang, J. E. Tepper, D. S. Hsu, T. Zhang, L. M. Reid, A. Z. Wang, *Nat. Biomed. Eng.* **2018**, *2*, 443; b) L. Varinelli, M. Guaglio, S. Brich, S. Zanutto, A. Belfiore, F. Zanardi, F. Iannelli, A. Oldani, E. Costa, M. Chighizola, E. Lorenc, S. P. Minardi, S. Fortuzzi, M. Filugelli, G. Garzone, F. Pisati, M. Vecchi, G. Pruneri, S. Kusamura, D. Baratti, L. Cattaneo, D. Parazzoli, A. Podestà, M. Milione, M. Deraco, M. A. Pierotti, M. Gariboldi, *J. Mol. Cell Biol.* **2022**, *14*, mjac064.
- [12] E. K. Michail, D. Hicham, M. Athanasios, in *Alginate*, (Ed: P. Leonel), IntechOpen, Rijeka **2019**.
- [13] a) R. R. Hatlen, P. Rajagopalan, *Acta Biomater.* **2021**, *132*, 421; b) S. K. Seidlits, Z. Z. Khaing, R. R. Petersen, J. D. Nickels, J. E. Vanscoy, J. B. Shear, C. E. Schmidt, *Biomaterials* **2010**, *31*, 3930; c) C. Wang, Q. Zhao, X. Zheng, S. Li, J. Chen, H. Zhao, F. Chen, L. Cui, W. Li, *Acta Biomater.* **2023**, *158*, 132.
- [14] X. Shao, I. N. Taha, K. R. Clauser, Y. Gao, A. Naba, *Nucleic Acids Res.* **2020**, *48*, D1136.
- [15] a) R. Simsa, T. Rothenbücher, H. Gürbüz, N. Ghosheh, J. Emneus, L. Jenndahl, D. L. Kaplan, N. Bergh, A. M. Serrano, P. Fogelstrand, *PLoS One* **2021**, *16*, e0245685; b) Y. Jin, J. S. Lee, J. Kim, S. Min, S. Wi, J. H. Yu, G.-E. Chang, A.-N. Cho, Y. Choi, D.-H. Ahn, *Nat. Biomed. Eng.* **2018**, *2*, 522; c) A.-N. Cho, Y. Jin, Y. An, J. Kim, Y. S. Choi, J. S. Lee, J. Kim, W.-Y. Choi, D.-J. Koo, W. Yu, *Nat. Commun.* **2021**, *12*, 4730.
- [16] a) H. Lin, G. Yang, J. Tan, R. S. Tuan, *Biomaterials* **2012**, *33*, 4480; b) A. J. Morwood, I. A. El-Karim, S. A. Clarke, F. T. Lundy, *Molecules* **2023**, *28*.
- [17] T. G. Phan, P. I. Croucher, *Nat Rev Cancer* **2020**, *20*, 398.
- [18] L. Saft, B. Timar, A. Porwit, *J Hematop* **2020**, *13*, 79.
- [19] C. Lee-Thedieck, P. Schertl, G. Klein, *Adv. Drug Del. Rev.* **2022**, *181*, 114069.
- [20] C. Zanetti, D. S. Krause, *Exp. Hematol.* **2020**, *89*, 13.
- [21] a) L. S. Steelman, S. C. Pohnert, J. G. Shelton, R. A. Franklin, F. E. Bertrand, J. A. McCubrey, *Leukemia* **2004**, *18*, 189; b) M. B. Miranda, D. E. Johnson, *Leukemia* **2007**, *21*, 1363; c) G. Poudel, M. G. Tolland, T. P. Hughes, I. S. Pagani, *Cancers (Basel)* **2022**, *14*; d) L. S. Steelman, S. L. Abrams, J. Whelan, F. E. Bertrand, D. E. Ludwig, J. Bäsecke, M. Libra, F. Stivala, M. Milella, A. Tafuri, P. Lunghi, A. Bonati, A. M. Martelli, J. A. McCubrey, *Leukemia* **2008**, *22*, 686.
- [22] a) Y.-W. Huang, W.-H. Lee, Y.-H. Tsai, H.-M. Huang, *Am. J. Physiol. Cell Physiol.* **2014**, *306*, C37; b) K. Naka, Y. Jomen, K. Ishihara, J. Kim, T. Ishimoto, E.-J. Bae, R. P. Mohney, S. M. Stirdivant, H. Oshima, M. Oshima, D.-W. Kim, H. Nakauchi, Y. Takihara, Y. Kato, A. Ooshima, S.-J. Kim, *Nat. Commun.* **2015**, *6*, 8039; c) C.-G. Wang, L. Zhong, Y.-L. Liu, X.-J. Shi, L.-Q. Shi, L. Zeng, B.-Z. Liu, *Integr Cancer Ther* **2016**, *16*, 526; d) L. Zhang, Z. Wang, T. Khishignyam, T. Chen, C. Zhou, Z. Zhang, M. Jin, R. Wang, Y. Qiu, D. Kong, *Biomed. Pharmacother.* **2018**, *103*, 1069; e) J.-H. Yen, C.-Y. Lin, C.-H. Chuang, H.-K. Chin, M.-J. Wu, P.-Y. Chen, *Cells* **2020**, *9*, 877; f) Y.-H. Kuo, S.-H. Wei, J.-H. Jiang, Y.-S. Chang, M.-Y. Liu, S.-L. Fu, C.-Y. F. Huang, W.-J. Lin, *Int. J. Mol. Sci.* **2021**, *22*, 12573; g) J. Yang, L. Chen, Y. Yan, J. Qiu, J. Chen, J. Song, Q. Rao, Y. Ben-David, Y. Li, X. Hao, *Biomed. Pharmacother.* **2019**, *112*, 108603.
- [23] a) A. Dutta, T. Sen, A. Chatterjee, *Int. J. Clin. Exp. Pathol.* **2010**, *3*, 288; b) D. Naci, M.-A. El Azreq, N. Chetoui, L. Lauden, F. Sigaux, D. Charron, R. Al-Daccak, F. Aoudjit, *J. Biol. Chem.* **2012**, *287*, 17065.
- [24] L. N. Eadie, T. P. Hughes, D. L. White, *PLoS One* **2016**, *11*, e0161470.
- [25] a) D. Naci, S. Berrazouane, F. Barabé, F. Aoudjit, *Sci. Rep.* **2019**, *9*, 19455; b) S. Berrazouane, M. Boisvert, S. Salti, W. Mourad, R. Al-Daccak, F. Barabé, F. Aoudjit, *Cell Death Dis.* **2019**, *10*, 357.
- [26] V. Münch, L. Trentin, J. Herzog, S. Demir, F. Seyfried, J. M. Kraus, H. A. Kestler, R. Köhler, T. F. E. Barth, G. te Kronnie, K.-M. Debatin, L. H. Meyer, *Blood* **2017**, *130*, 643.

- [27] N. Zhou, X. Yuan, Q. Du, Z. Zhang, X. Shi, J. Bao, Y. Ning, L. Peng, *Nucleic Acids Res.* **2023**, *51*, D571.
- [28] C. Zhang, X. Liu, S. Jin, Y. Chen, R. Guo, *Mol Cancer* **2022**, *21*, 47.
- [29] X. Liu, Y. Zhang, X. Wu, F. Xu, H. Ma, M. Wu, Y. Xia, *Front Pharmacol* **2022**, *13*, 909821.
- [30] a) E. Grignano, L. Cantero-Aguilar, Z. Tuerdi, T. Chabane, R. Vazquez, N. Johnson, J. Zerbit, J. Decroocq, R. Birsén, M. Fontenay, O. Kosmider, N. Chapuis, D. Bouscary, *Cell Death Discov* **2023**, *9*, 97; b) Y. Yu, Y. Meng, X. Xu, T. Tong, C. He, L. Wang, K. Wang, M. Zhao, X. You, W. Zhang, L. Jiang, J. Wu, M. Zhao, *ACS Nano* **2023**, *17*, 3334; c) X. Liu, S. Zhong, K. Qiu, X. Chen, W. Wu, J. Zheng, Y. Liu, H. Wu, S. Fan, D. Nie, X. Wang, Z. Yu, Z. Liao, M. Zhong, Y. Li, C. Zeng, *Exp Hematol Oncol* **2023**, *12*, 47.
- [31] M. L. MacDonald, I. V. J. Murray, P. H. Axelsen, *Biol. Med.* **2007**, *42*, 1392.
- [32] a) X. Sun, X. Niu, R. Chen, W. He, D. Chen, R. Kang, D. Tang, *Hepatology* **2016**, *64*, 488; b) M. Satoh, M. G. Cherian, N. Imura, H. Shimizu, *Cancer Res.* **1994**, *54*, 5255.
- [33] a) Y. Jin, J. S. Lee, J. Kim, S. Min, S. Wi, J. H. Yu, G.-E. Chang, A.-N. Cho, Y. Choi, D.-H. Ahn, S.-R. Cho, E. Cheong, Y.-G. Kim, H.-P. Kim, Y. Kim, D. S. Kim, H. W. Kim, Z. Quan, H.-C. Kang, S.-W. Cho, *Nat. Biomed. Eng.* **2018**, *2*, 522; b) A.-N. Cho, Y. Jin, Y. An, J. Kim, Y. S. Choi, J. S. Lee, J. Kim, W.-Y. Choi, D.-J. Koo, W. Yu, G.-E. Chang, D.-Y. Kim, S.-H. Jo, J. Kim, S.-Y. Kim, Y.-G. Kim, J. Y. Kim, N. Choi, E. Cheong, Y.-J. Kim, H. S. Je, H.-C. Kang, S.-W. Cho, *Nat. Commun.* **2021**, *12*, 4730.
- [34] Y. Perez-Riverol, J. Bai, C. Bandla, D. García-Seisdedos, S. Hewapathirana, S. Kamatchinathan, D. J. Kundu, A. Prakash, A. Frericks-Zipper, M. Eisenacher, M. Walzer, S. Wang, A. Brazma, J. A. Vizcaino, *Nucleic Acids Res.* **2022**, *50*, D543.
- [35] B. Langmead, S. L. Salzberg, *Nat. Methods* **2012**, *9*, 357.
- [36] A. R. Quinlan, I. M. Hall, *Bioinformatics* **2010**, *26*, 841.
- [37] R. C. Gentleman, V. J. Carey, D. M. Bates, B. Bolstad, M. Dettling, S. Dudoit, B. Ellis, L. Gautier, Y. Ge, J. Gentry, K. Hornik, T. Hothorn, W. Huber, S. Iacus, R. Irizarry, F. Leisch, C. Li, M. Maechler, A. J. Rossini, G. Sawitzki, C. Smith, G. Smyth, L. Tierney, J. Y. H. Yang, J. Zhang, *Genome Biol.* **2004**, *5*, R80.